

Geometrical frustration effects on charge-driven quantum phase transitions

L. Cano-Cortés,¹ A. Ralko,² C. Février,² J. Merino,¹ and S. Fratini²

¹*Departamento de Física Teórica de la Materia Condensada,
Universidad Autónoma de Madrid, Madrid 28049, Spain*

²*Institut Néel-CNRS and Université Joseph Fourier,
Boîte Postale 166, F-38042 Grenoble Cedex 9, France*

(Dated: April 24, 2022)

The interplay of Coulomb repulsion and geometrical frustration on charge-driven quantum phase transitions is explored. The ground state phase diagram of an extended Hubbard model on an anisotropic triangular lattice relevant to quarter-filled layered organic materials contains homogeneous metal, 'pinball' and three-fold charge ordered metallic phases. The stability of the 'pinball' phase occurring for strong Coulomb repulsions is found to be strongly influenced by geometrical frustration. A comparison with a spinless model reproduces the transition from the homogeneous metallic phase to a pinball liquid, which indicates that the spin correlations should play a much smaller role than the charge correlations in the metallic phase close to the charge ordering transition. Spin degeneracy is, however, essential to describe the dependence of the system on geometrical frustration. Based on finite temperature Lanczos diagonalization we find that the effective Fermi temperature scale, T^* , of the homogeneous metal vanishes at the quantum phase transition to the ordered metallic phase driven by the Coulomb repulsion. Above this temperature scale 'bad' metallic behavior is found which is robust against geometrical frustration in general. Quantum critical phenomena are not found whenever nesting of the Fermi surface is strong, possibly indicating a first order transition instead. 'Reentrant' behavior in the phase diagram is encountered whenever the $2k_F$ -CDW instability competes with the Coulomb driven three-fold charge order transition. The relevance of our results to the family of quarter-filled materials: θ -(BEDT-TTF)₂X is discussed.

PACS numbers: 71.27.+a,74.40.Kb,71.30.+h,71.45.Lr

I. INTRODUCTION

Strongly correlated electron materials are often characterized by complex phase diagrams, reflecting an intricate interplay between magnetic, orbital, lattice and charge degrees of freedom. As these excitations couple to the conduction electrons, the metallic state expected in the absence of interactions has to compete with several ordered phases. Examples of these materials include cuprate superconductors, nickelates, heavy fermion compounds, transition metal dichalcogenides, organic charge transfer salts and the iron based pnictide superconductors, all presenting various forms of magnetic, orbital and charge order. Even when a metallic phase is stabilized, these systems are generally found to exhibit large effective mass enhancements and electrical resistivities violating the Ioffe-Regel-Mott (IRM) condition¹⁻⁶. Surprisingly enough, such "bad" metallic behavior does not impede the emergence of superconductivity, but rather appears to be a prerequisite for the achievement of high critical temperatures⁷.

Charge ordered (CO) phases are commonly observed in the class of two-dimensional organic compounds θ -ET₂X (ET=BEDT-TTF, bisethylenedithio-tetrafulvalene)⁸⁻¹², and ascribed to the prominent role of electron-electron interactions¹³. At the non-interacting level, these compounds are predicted to be metals with 3/4-filled electronic bands. The observation of electronic ordering implies that the magnitude of electron-electron interactions is comparable with the widths of the relevant electronic

bands constructed from the π molecular orbitals. In turn, the presence of such strong interactions raises questions about the nature of the metallic phase in these materials, that should exhibit distinctive features of "correlated electron systems" in the Mott sense. The proximity to charge ordering instabilities, with the possible emergence of quantum critical points as the transition temperature is made to vanish, is also expected to strongly alter the physical properties of the metal. All these ingredients should lead to measurable deviations from the usual Fermi liquid behavior^{14,15}, in close analogy with heavy fermion systems¹⁶⁻¹⁹.

The minimal theoretical description of the electronic properties of θ -ET₂X organic conductors is based on the two-dimensional extended Hubbard model (EHM) on a triangular lattice. Several theoretical studies have aimed at reproducing the different CO patterns realized in this class of materials, either within the framework of the EHM itself or its generalizations, including longer ranged electronic interactions and various types of electron-lattice interactions^{20,21}. In the present work we focus on the following open issues: (i) how does the strength of the local Coulomb correlations modify the nature of the metallic phase as well as its CO instabilities, (ii) what are the effects of geometrical frustration in the electron motion arising from the triangular molecular arrangement, and (iii) how does the proximity to a given CO phase extend its influence onto the properties of the correlated metal, possibly leading to non-Fermi liquid behavior?

In Sec. II we set the minimal electronic model needed

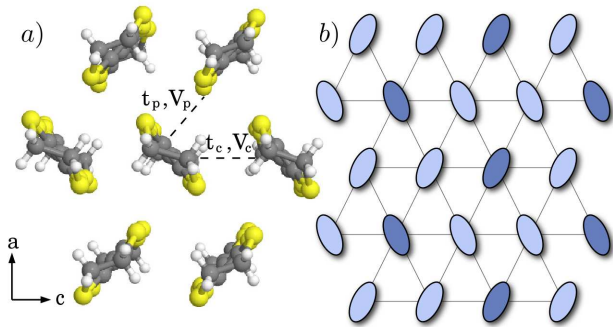


FIG. 1: (Color online) (a) Arrangement of BEDT-TTF molecules in the conducting layers of θ -type ET crystals, with the corresponding transfer integrals and nearest-neighbor Coulomb interactions. (b) Threefold charge ordered phase in the triangular lattice considered in this work. The triangular lattice is defined by the real space unit vectors $\mathbf{a}_1 = (1, 0)$ defining the c direction and $\mathbf{a}_2 = (1/2, \sqrt{3}/2)$.

for the study of electronic properties of θ -(ET) $_2$ X compounds and provide a brief review of established theoretical results. In Sec. III the model is solved by Lanczos diagonalization and the zero-temperature phase diagram is obtained for different degrees of geometrical frustration. In Sec. IV the resulting metallic phases are explored through a finite- T Lanczos diagonalization calculation^{22–24}. We theoretically explore the consequences of a quantum critical point (QCP) at a charge ordering transition driven by the quantum fluctuations associated with strong inter-site Coulomb repulsion. Our results are compared with a spinless calculation in order to assess the importance of the magnetic degrees of freedom in the observed quantum criticality and make contact with the existing literature. The relevance of the present results to the physics of θ -type ET compounds is discussed in the conclusive Sec. V.

II. MODEL AND METHOD

1. Extended Hubbard model on the triangular lattice

Quasi two-dimensional organic conductors (general formula A_2B) are charge transfer compounds composed of alternating layers of conducting (donor) molecules A and insulating (acceptor) units B . They exhibit a large variety of molecular arrangements corresponding to different polytypes classified by greek characters^{13,25}. The materials of the θ -ET $_2$ X class have a triangular lattice structure, shown in Fig. 1, with an average of $n = 3/2$ electrons per molecule, fixed by complete charge transfer between A and B units. Since this corresponds to a three-quarter filled electronic band, these materials should be normal metals in the absence of interactions.

The electronic properties of θ -ET $_2$ X materials are

commonly described via the extended Hubbard Model (EHM),

$$H = -t_p \sum_{\langle ij \rangle_{p\sigma}} (c_{i\sigma}^\dagger c_{j\sigma} + H.c.) - t_c \sum_{\langle ij \rangle_{c\sigma}} (c_{i\sigma}^\dagger c_{j\sigma} + H.c.) + U \sum_i n_{i\uparrow} n_{i\downarrow} + V_p \sum_{\langle ij \rangle_p} n_i n_j + V_c \sum_{\langle ij \rangle_c} n_i n_j. \quad (1)$$

This model includes transfer integrals between the π -orbitals of nearest-neighboring molecules in the conducting plane, labeled by t_p and t_c according to the bond directions, a local (on-site) Coulomb repulsion energy U as well as non-local (nearest-neighbor) repulsion terms V_c, V_p (see Fig. 1)⁷¹.

Early mean-field calculations^{26–28} indicated that three types of striped patterns (vertical, diagonal and horizontal) are realized depending on the relative magnitude of the non-local Coulomb interaction parameters. These results were later confirmed by more advanced numerical techniques that can properly account for electronic correlations, such as exact diagonalization (ED)^{29,30} and density matrix renormalization group (DMRG)³¹.

More interesting from our perspective is the isotropically interacting case, $V_p = V_c \equiv V$ ^{20,27,28,31–35}. There, because of the frustration of inter-molecular interactions induced by the triangular lattice geometry, an alternative charge ordering pattern with three-fold periodicity is favored with respect to the (degenerate) striped arrangements, illustrated in Fig. 1b. A more exotic situation is found in the limit of strong local Coulomb interactions (or, similarly, in a fully spin polarized electron system, i.e. for spinless electrons), where the constraint of no double occupancy on molecular sites converts this three-fold order into a partially ordered phase termed "pinball liquid" (PL)^{15,31,33,35}: this state shows a three-sublattice structure with the same symmetry as the threefold phase, in which the carriers of one sublattice are essentially localized as a Wigner-crystal (pin), with the remaining charges (balls) forming an itinerant liquid on the interstitials. It is not clear at present how the transition between these two qualitatively different forms of threefold order takes place as a function of the local Coulomb repulsion U . This issue will therefore be thoroughly discussed here.

In addition to the effects of the local electronic correlations, we are interested in the effects of geometrical frustration in the electronic motion, that are triggered by the strongly directional π -overlaps between neighboring molecules⁷². This issue is of particular importance to actual materials, as the relative values of the transfer integrals t_c and t_p can be tuned experimentally by applying pressure or by chemical substitution, which modifies the relative angles between neighboring molecules^{36,37}. As a general observation, negative values of the ratio t_c/t_p produce the highest charge ordering temperatures^{20,36}, while vanishing or positive values lead to glassy ($X=\text{CsCo}(\text{SCN})_4$, $X=\text{CsZn}(\text{SCN})_4$)³⁸ or even superconducting ($X=\text{I}_3$) ground states^{20,36,39}. From a more theoretical point of view, how the system evolves

from a perfectly isotropic triangular lattice at $t_c = \pm t_p$ to a square lattice at $t_c = 0$ remains an open issue.

Transfer integrals obtained through the Hückel approximation in quarter-filled θ -ET crystals are in the range: $-0.5 \lesssim t_c/t_p \lesssim 1.5$, with $t_p \approx -0.05 - 0.1 \text{ eV}^{37}$. These values generally differ from the ones extracted from optical reflectivity and de Haas Van Alphen experiments³⁹ for each specific crystal. On the other hand, Coulomb repulsion energies in organic molecular crystals⁴⁰ have been estimated by calculating the screening corrections to the bare repulsion energies of the isolated molecules, U_0 and V_0 , obtained from *ab initio* calculations⁴¹. These calculations lead to Hubbard parameters of the model Eq. (1): $U \sim U_0/2 \sim (15 - 20)|t_p|$, and $V_p \sim V_c \sim U/2$, with a bandwidth $W \sim (8 - 9)|t_p|$. These Coulomb energies are larger than assumed in previous works^{30,31,35,42}: $U \sim (8 - 10)|t_p|$, and $V \sim (1 - 3)|t_p|$, as extracted from optical reflectivity measurements¹³. The degree of uncertainty in the microscopic parameters implies that a general understanding of the model and its phase diagram in the full parameter space U , V and t_c/t_p is essential. This is the main focus of the present work.

2. Finite- T Lanczos approach

We perform ED calculations through a finite- T Lanczos algorithm with periodic boundary conditions^{22,23}. The large number of excited states inherent to the many-body problem which are needed to evaluate statistical sums is cutoff by keeping only a small number of low lying states at each temperature. This is performed through an Arnoldi algorithm²⁴ which reduces the size of the Hilbert space enormously. The accuracy of the method is restricted to temperatures which are not too low, i.e. not lower than the energy of the lowest excitation of the quantum many-body system. For the method to be practical T should not be too large that one needs to keep too many states in the statistical sums. Finite-size effects are somewhat reduced by the effect of temperature and the method is quite reliable for extracting integrated properties. Instead, spectral properties such as optical conductivity and photoemission spectra are prone to large finite size effects, and will not be analyzed here.

Due to the high computational demand of the finite- T algorithm, the calculations are performed on an $N_s = 12$ site cluster. In principle, a larger $N_s = 18$ cluster whose geometry is also suitable for reproducing the three-fold CO pattern could be used at $T = 0$. However, we shall not consider such case because a 3/4-filling implies a different number of spin up and spin down electrons, while the ground state is expected to be in a $S = S_z = 0$ state.

We characterize the physical properties of the different phases based on the following quantities, that are accessible through finite- T Lanczos calculations.

(i) *Charge correlation function*: The charge structure factor signalling the possible occurrence of a charge or-

dered state in the system is evaluated at finite- T through:

$$C(\mathbf{q}) = \frac{1}{Z} \sum_m e^{-\beta E_m} \langle m | \frac{1}{N_s} \sum_{i,j} e^{i\mathbf{q}\cdot\mathbf{R}_{ij}} n_i n_j | m \rangle. \quad (2)$$

Here $Z = \sum_m e^{-\beta E_m}$ is the partition function of the system and $\beta = 1/k_B T$. A charge ordered state with modulation \mathbf{Q} is signalled if $C(\mathbf{Q})$ is finite in the thermodynamic limit. The three-fold ordering corresponds to a charge density modulation with wavevector $\mathbf{Q} = (2\pi/3, 2\pi/\sqrt{3})$, which lies at the corner of the hexagonal Brillouin zone, see Fig. 11 (all corners are equivalent, being connected by reciprocal lattice vectors or time-reversal symmetry). An accurate numerical determination of the phase boundaries should rely on a proper finite-size scaling of the results. While this is prohibitive for the fermionic system under study due to the rapidly increasing size of the Hilbert space, the ordering transitions can still be identified as the locus of steepest variation of charge correlations upon varying the microscopic parameters of the model.

(ii) *Kinetic energy*: This quantity provides direct information on how the motion of the charge carriers is slowed down by interactions. It can be evaluated with high accuracy from the finite- T Lanczos diagonalization, because it results from a quantum mechanical and thermal average over a huge number of states. By normalizing it to a reference non-interacting value K_0 , it gives valuable information on the degree of electronic correlations in the many-body system^{43,44}. Under suitable assumptions, this quantity can be compared with optical absorption experiments in actual materials via the f-sum rule⁴⁵.

The kinetic energy is evaluated from the following thermal average,

$$K = \frac{1}{Z} \sum_m e^{-\beta E_m} \langle m | \frac{1}{N_s} \sum_{\mathbf{k},\sigma} \epsilon_{\mathbf{k}} c_{\mathbf{k}\sigma}^\dagger c_{\mathbf{k}\sigma} | m \rangle, \quad (3)$$

where $|m\rangle$ is the total set of eigenstates of the system with energies E_m .

(iii) *Double occupancy*: It is useful to analyze the number of double occupancy per site in the lattice which reads:

$$d = \sum_m e^{-\beta E_m} \langle m | \frac{1}{N_s} \sum_i n_{i\uparrow} n_{i\downarrow} | m \rangle, \quad (4)$$

and is different for the different phases analyzed. For example, it is a key quantity in the analysis of the Mott transition in the half-filled Hubbard model since d is suppressed in the Mott insulator, which allows to determine the critical Coulomb coupling. In model Eq. (1), d is helpful for characterizing the different possible CO states for different U and V .

(iv) *Specific heat*: From the total energy of the system, $E = \langle H \rangle$, we can obtain the specific heat by taking the derivative with respect to the temperature, T :

$$C_V = \frac{\partial \langle H \rangle}{\partial T}. \quad (5)$$

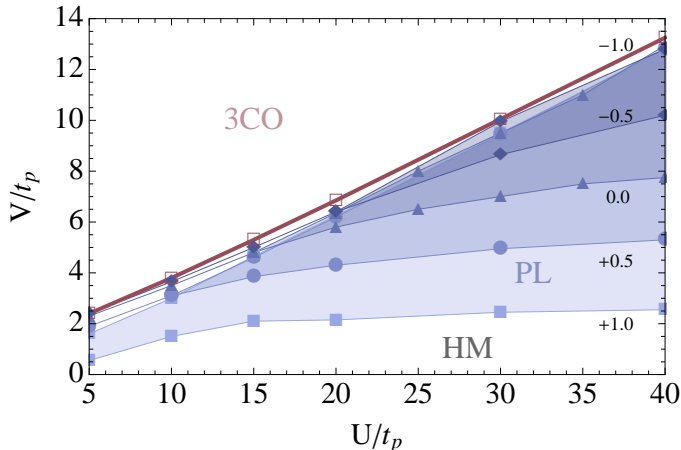


FIG. 2: (Color online) Phase diagram obtained at $T = 0$ from numerical diagonalization of a $N_s = 12$ cluster. The different shaded areas correspond to the pinball (PL) phase for $t_c/t_p = 1, 0.5, 0, -0.5$ (squares, circles, triangles, diamonds respectively, from light to dark blue). The case $t_c/t_p = -1$ has no pinball phase in the explored U range. The red line corresponds to a direct transition from the homogeneous metal (HM) or pinball liquid (PL) to the threefold charge ordered (3CO) state.

Unless otherwise specified, we use units such that $k_B = \hbar = 1$. The finite temperature method recovers the ground state properties by taking the limit: $\beta \rightarrow \infty$. In practice this is achieved for $\beta = 50 - 100$ for the various U and V explored across the whole phase diagram. Typically about 30 to 50 terms are kept in the evaluation of the statistical sums over the excited states $|m\rangle$ with corresponding energies E_m .

III. PHASE DIAGRAM AT T=0

The zero temperature phase diagram of the model Eq. (1) in the (U, V) plane is shown in Fig. 2. The phase transition lines are determined using three alternative methods, that all give coincident results: (i) via the evolution of the charge correlation function $C(\mathbf{Q})$ calculated at the three-fold wavevector, Fig. 3; (ii) by tracking directly the charge ordering patterns that develop in real space, Fig. 4; and (iii) by analyzing the *fidelity* between groundstates at different values of the microscopic parameters, Fig. 5, as introduced below.

We are interested here in the charge ordering instabilities driven by the inter-site repulsion V . Our numerical results confirm the existence of three distinct phases: a homogeneous metal (HM) at low V , a three-fold charge ordered phase (3CO) at large V , and an intermediate “pinball liquid” (PL) phase emerging at large values of U . The most striking effect in Fig. 2 is that the region of the homogeneous metallic phase is strongly reduced upon increasing the t_c/t_p ratio, evidently due to a corresponding stabilization of the competing pinball liquid

phase. We note that the homogeneous metal is always the ground state at $V = 0$ independently of the strength of the local repulsion U . This can be rationalized by the fact that in the absence of nearest-neighbor interactions, at $n = 3/2$ the holes ($n_h = 2 - n = 1/2$) can effectively avoid each other when moving along the lattice.

A. Characterization of the different phases

Fig. 3 reports the evolution of the charge correlation function, the kinetic energy and double occupancy as a function of V , along vertical cuts in the phase diagram corresponding to $U/t_p = 5$ and $U/t_p = 40$. Different curves correspond to different values of t_c/t_p (upper and lower panels, respectively).

1. Small U : HM to 3CO transition

At low U , the instability towards the threefold charge ordered phase is signaled by a sharp jump in the correlation function (Fig. 3a), starting from a small constant value in the homogeneous metal. The locus of the 3CO transition shows an appreciable dependence on geometrical frustration: the homogeneous metal is rapidly destabilized for positive values of t_c/t_p , in marked contrast with the weaker (and opposite) variations expected from an RPA analysis valid in the weakly correlated limit²⁸ (see Appendix A). From the phase diagram of Fig. 2 it is quite clear that this trend is governed by a mechanism that extends from the strongly correlated limit $U \gg t_p$ down to the lowest values of U . The emergence of an intermediate plateau in the charge correlation function, clearly visible in the data at $t_c = t_p$ in Fig. 3a, is also reminiscent of the situation encountered at $U/t_p = 40$ (see below). These observations suggest that the presence of geometrical frustration, $t_c/t_p > 0$, strongly enhances the role of electronic correlations. The pinball phase characteristic of strong U is stabilized at $t_c = t_p$ despite a relatively low nominal value $U/t_p = 5$.

We note that the nature of the ordering transition changes in the opposite limiting case $t_c = -t_p$, where the sharp jump in the correlation function is replaced by a smoother evolution, possibly due to the competition with an incipient nesting instability (Appendix A).

The behavior of the charge correlation function is directly mirrored in the other physical quantities shown in Figs. 3. The kinetic energy (Fig. 3c) jumps at the phase transition from an essentially free-electron value, $K/K_0 \gtrsim 0.9$, to a value that is reduced by the opening of the charge ordering gap. At the same time, the double occupancy (Fig. 3e) undergoes a marked increase towards the value $d = 0.66$ of the fully formed 3CO: the charge is ordered into three sublattices with average occupations $n_A = n_B = 2$ and $n_C = 1/2$ (see Fig. 4, large V region), so that each of the two charge rich sublattices contributes $d_A = d_B = 1/3$ to the average double occu-

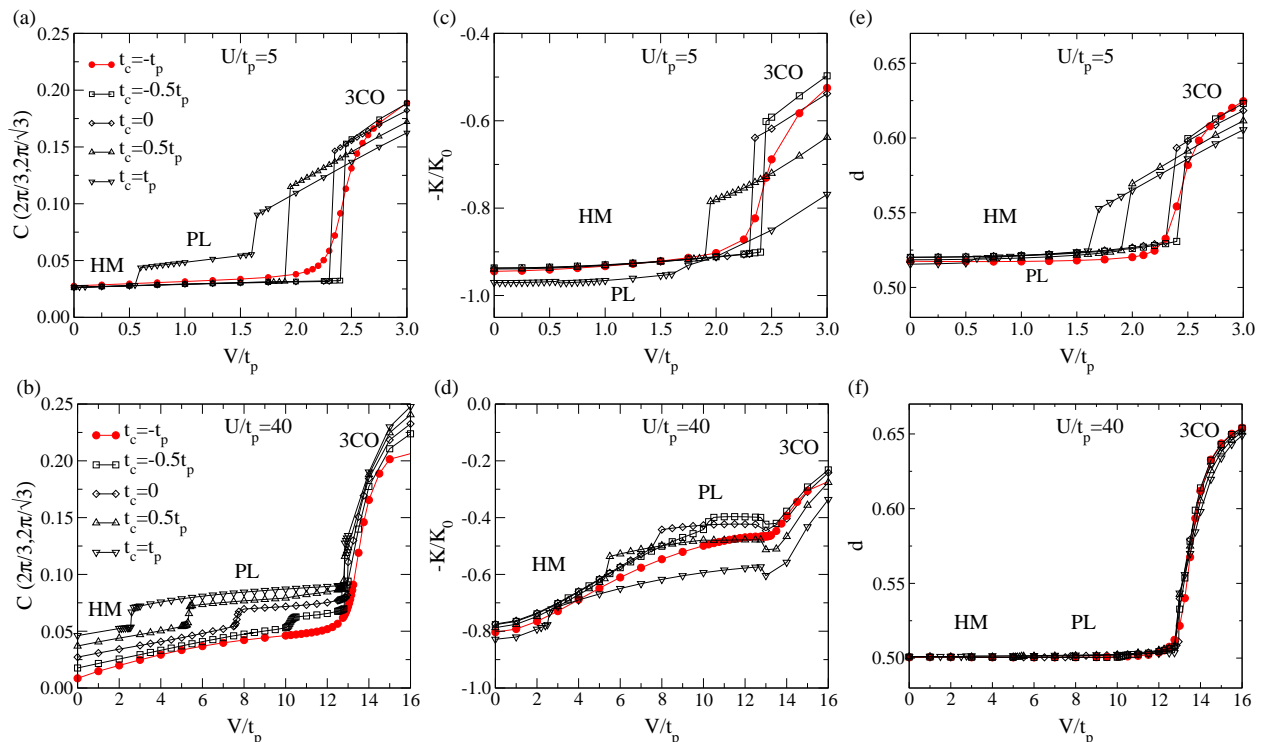


FIG. 3: (Color online) (a)-(b) Charge correlation function for the threefold wavevector $\mathbf{Q} = (2\pi/3, 2\pi/\sqrt{3})$ as a function of V/t_p (a) in the weakly correlated $U = 5t_p$ and (b) the strongly correlated limit $U = 40t_p$. (c)-(d) Average normalized kinetic energy K/K_0 as a function of V/t_p . (e)-(f) Double occupancy probability. The plots in (b) have a vertical offset of ± 0.02 for $t_c = \pm t_p$ and of ± 0.01 for $t_c \pm 0.5t_p$ for clarity.

pancy. The fact that the double occupancy in the homogeneous metal is suppressed from the non-interacting value $d = (n/2)^2 = (3/4)^2 = 0.5625$ indicates the presence of moderate electronic correlations.

2. Large U : HM to PL transition

A richer situation is found in the large U regime. First of all, the homogeneous liquid is characterized by a total suppression of double occupancy: introducing the double occupancy of holes $d_h = \langle (1 - n_{i\uparrow})(1 - n_{i\downarrow}) \rangle = 1 - n + d$ and setting $d_h = 0$ we obtain $d = n - 1 = 1/2$, which is actually observed in Fig. 3f. Furthermore, the presence of both local and non-local Coulomb interactions hinders the particle motion, resulting in a marked reduction of the kinetic energy upon increasing V . An approximate expression for its V -dependence is:

$$K^{(HM)} \approx (1 - AV^2)K_U^{(HM)}, \quad (6)$$

where $K_U^{(HM)}$ is the value at $V = 0$. This V^2 dependence is consistent with a previous slave-boson⁴⁶ calculation of the metallic phase formed by spinless particles on a d -dimensional hypercubic lattice, which is compatible with the data of Fig. 3d. Because the ordering instability is pushed to large values of V for negative values of t_c/t_p (cf.

Fig. 2), the homogeneous metal that is so revealed can acquire quite a strongly correlated character, as testified by a kinetic energy ratio that decreases down to $K/K_0 \simeq 0.5$ before the onset of charge order.

The numerical data of Figs. 3b and d show quite clearly that an intermediate phase emerges between the homogeneous metal and the 3CO, that we associate with the pinball liquid phase introduced by Hotta and coworkers^{33,34,47}. The PL is a partially ordered phase with a three-sublattice structure, in which the carriers of one sublattice (pins) are localized as a Wigner-crystal and the remainder (balls) form an essentially non-interacting liquid within the resulting hexagonal lattice (Fig.1b).

To get a further insight about the different broken symmetry phases, we have calculated the static density profile in the presence of a local perturbation breaking all the translations of the lattice, but respecting the $\pi/3$ rotation. In this way, instead of obtaining a uniform linear combination of all symmetry related crystal states, the system selects one crystal state favored by the perturbation, giving access to a real-space snapshot of the broken-symmetry ground state. The basis of the method employed for getting the real space snapshot of the local densities is the following: we add a local potential on certain sites related by rotations in such a way that only translations are broken. The value of the local defects is

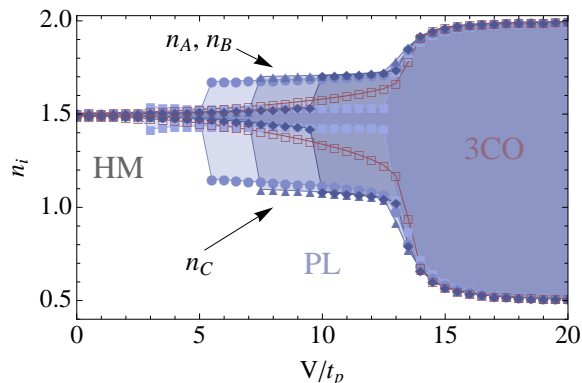


FIG. 4: (Color online) Average electron densities in the electron rich (hole poor, $n_A = n_B \geq n$, upper curves) and electron poor (hole rich, $n_C \leq n$, lower curves) sublattices, as obtained from Lanczos diagonalization at $U/t_p = 40$ in the presence of a weak translational symmetry breaking potential. We take $\delta = +0.05t_p$ on the sites of the hole rich sublattice in order to select one realization of the threefold symmetry. Color codes are the same as in Fig. 2 (from light to dark blue: $t_c/t_p = 1, 0.5, 0, -0.5$, red: $t_c/t_p = -1$).

few percents of the hopping term. In the Hamiltonian, we simply add the perturbation term: $\delta \sum_i (n_{i\uparrow} + n_{i\downarrow})$. This method has previously been used for distinguishing the exact nature of two phases breaking the translational and the rotational symmetries differently⁴⁸. Since the additional term is kept very small, it only corresponds to a perturbation and do not change the main property of the ground state. In this paper, we do want to keep the rotational symmetry safe, we hence chose 4 sites, in the 12-site cluster, in such a way that the system is still rotationally invariant. The perturbation has to be lower than the typical energy scale and we put $\delta = +0.05t_p$ on the sites of the hole rich sublattice. Results are depicted in Fig. 4. Expressing the charge densities in terms of holes, $n_h = 2 - n = 1/2$ and starting from the 3CO phase ($n_{h,A} = n_{h,B} = 0$ and $n_{h,C} = 3/2$, Fig. 4), by progressively increasing the local repulsion U , it becomes energetically unfavorable to accommodate more than one hole per molecule. Part of the hole density will then tend to spill out of the hole-rich sites in order to prevent double occupancy, resulting in $n_{h,C} = 1$. The average charge density in the three sublattices, $n_A = n_B = 7/4$, $n_C = 1$, illustrated in Fig. 4 indeed corresponds to a scenario where one sublattice is occupied by localized holes ($n_{h,C} = 1$ leading to $n_C = 2 - n_{h,C} = 1$) with the remaining particles equally spread in the interstitial sites ($n_{h,A} = n_{h,B} = n_{ball} = 1/4$ hole per site, leading to $n_A = n_B = 2 - n_{ball} = 7/4$). The critical value for the transition from 3CO to PL can be readily estimated to be $U \simeq 3V$ from electrostatic considerations alone (see Appendix B), and is therefore independent of t_c/t_p .

Notably, in the PL phase the physical quantities whose V dependence is depicted in Fig. 3 form well defined plateaus, suggesting that they are locked as a conse-

quence of the spontaneous separation between localized and itinerant charges. For example, the charge correlation function tends to the value $C(\mathbf{Q}) = n^2/3 \simeq 0.08$ instead of the full $C(\mathbf{Q}) = n^2$ obtained at complete ordering in the large V limit, corresponding to the fact that only 1/3 of the particles participate to the ordering phenomenon.

From our numerical results in Fig. 3d, the kinetic energy of both the homogeneous metal at $V < V_{PL}$ and the 3CO phase at $V > V_{3CO}$ is found to depend only weakly on the degree of geometrical frustration t_c/t_p . On the other hand, the kinetic energy forms a plateau within the PL phase, at a value which is strongly dependent on t_c/t_p : the absolute value of the (negative) kinetic energy in the PL phase is lowest at $t_c = -0.5t_p$ and its magnitude steadily increases as the frustration ratio is increased to $t_c = t_p$. Our data therefore suggest that it is this gain in kinetic energy for positive values of the geometrical frustration ratio that is responsible for the stabilization of the pinball liquid phase against the homogeneous metal observed in Fig. 2.⁷³ We note that a kinetic energy driven mechanism for the PL transition was also pointed out in Ref. 34. Since the effective filling associated with the itinerant balls on the hexagonal lattice is only $n_{ball} = 1/8$, Coulomb interaction effects are small. Indeed, we have checked that the kinetic energy of the balls coincides with the kinetic energy of the corresponding non-interacting tight-binding model on a hexagonal lattice, at filling $n = n_{ball}$, as a function of the ratio t_c/t_p .

B. Fidelity analysis

In order to characterize the quantum phase transitions of our system, the simple yet powerful concept of *fidelity*⁴⁹ is considered here (Fig. 5). Initially introduced in quantum information, the fidelity has revealed successful in determining superfluid-insulator transitions of the Hubbard model⁵⁰⁻⁵². The idea behind the fidelity is very simple; it consists of computing overlaps of ground states (GS) $|\psi_0\rangle$ at different values of the microscopic parameters. At a QCP, even the smallest change of the parameters can have dramatic effects in some of the observables. This is encoded in the GS properties, hence, the overlap is expected to strongly react and indicate the locations of the phase transitions. We define the fidelity F as:

$$F_{V,V'} = |\langle \psi_0(V') | \psi_0(V) \rangle|. \quad (7)$$

Obviously, for $V = V'$, the fidelity should be $F_{V,V} = 1$. Typical results are depicted in Fig. 5 at $U = 40t_p$, and for five values of $t_c/t_p = \pm 1.0, \pm 0.5$ and 0.0 .

It is surprising to see how the fidelity is indeed able to pinpoint the phase transitions. For each of the values of t_c/t_p , we exactly recover the transitions obtained by more standard methods in the preceding Sections. More information is available, however. First, there is always

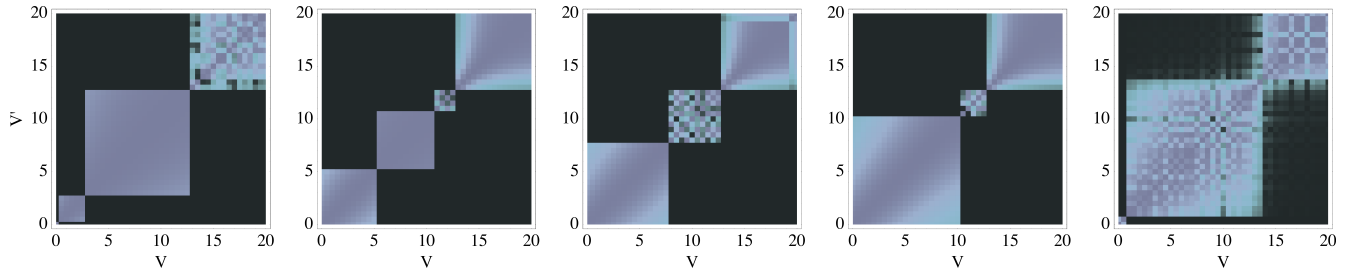


FIG. 5: (Color online). Fidelity $F_{V,V'} = |\langle \psi_0(V') | \psi_0(V) \rangle|$ for various values of t_c/t_p , from left to right 1.0, 0.5, 0.0, -0.5 and -1.0 and $U = 40|t_p|$. There is a perfect agreement with the phase transitions obtained by standard quantities (order parameters, kinetic energies, susceptibilities). The case of zero overlap is represented in black, while the blue-violet (diagonal squares) represents overlap 1 ($V=V'$). The non-uniform colored zones stand for fluctuating ground states possibly related to a strong degeneracy.

some region where F is strongly fluctuating, even though well delimited in the (V, V') plane (non uniform colored zones). These fluctuations can be due to a large degeneracy of the GS hence corresponding to a same order but with destructive interferences. The second important information is visible in the case $t_c/t_p = 0.5$, where the fidelity indicates the existence of two distinct phases in the pinball region [namely $5.20(2) \leq V/t_p \leq 11.00(2)$ and $11.00(2) \leq V/t_p \leq 13.00(2)$], suggesting a possible ordering of the mobile charges. In fact, a slight change in the kinetic energy (Fig. 3d) appears at this transition, but the other quantities seem to be insensitive to it. The fact that the transition within the pinball phase is not detected by the charge correlation function (Fig. 3b) nor by the average densities (Fig. 4) tends to show that their properties remain extremely close. Nevertheless, the fidelity F allows a precise determination of the sub-phases.

C. Spinless model

We now consider the spinless version of the model Eq. (1), which has been discussed extensively in the literature^{33,34,47,53}. Since the spinless model only contains charge degrees of freedom, by comparing it with the spinful model we can obtain useful information on the relative role played by charge fluctuations as compared to the spin fluctuations.

The spinless model reads:

$$\begin{aligned}
 H = & t_p \sum_{\langle ij \rangle_p} \left(h_i^\dagger h_j + H.c. \right) + t_c \sum_{\langle ij \rangle_c} \left(h_i^\dagger h_j + H.c. \right) \\
 & + V_p \sum_{\langle ij \rangle_p} n_i n_j + V_c \sum_{\langle ij \rangle_c} n_i n_j, \quad (8)
 \end{aligned}$$

where we have changed the sign of the hopping integrals to deal explicitly with holes. As in the preceding Sections we consider the case $V_c = V_p = V$ for different values of the t_c/t_p ratio. Importantly, for spinless particles the physical situation of one hole per two sites implies a half-filled band, which gives rise to a spurious particle-hole

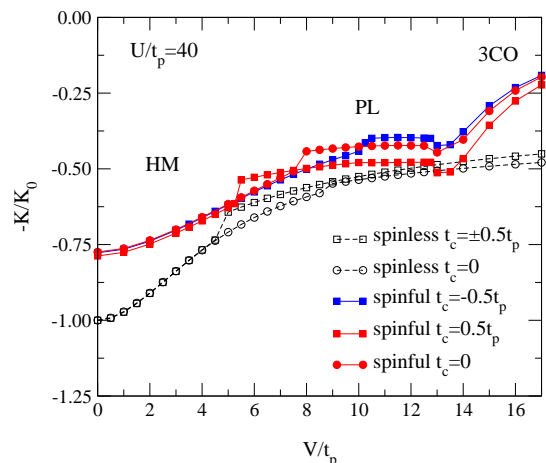


FIG. 6: (Color online) Dependence of the kinetic energy on V for the spinless and spinful extended Hubbard models. Different t_c/t_p ratios are compared in the two situations. As expected, the properties of the spinless model are independent of the sign of t_c/t_p , in contrast to the spinful model.

invariance that is absent in the spinful case at $3/4$ -filling. Therefore, the thermodynamic properties as well as the phase transition lines become invariant under a change of sign of t_c/t_p .

In Fig. 6 we show the V -dependence of the kinetic energy for different t_c/t_p ratios compared with the spinful model. As expected the figure shows how the kinetic energy in the spinless model does not depend on the sign of t_c/t_p (black curves). The spinless model is able to recover the qualitative trends of the full model for $t_c/t_p \geq 0$: the critical values at which the transition from the HM to the PL occurs are respectively $V_{PL} \simeq 4.5t_p$ and $8.5t_p$ for $t_c/t_p = 0.5$ and 0 in the spinless case, to be compared with $V_{PL} \simeq 5.5t_p$ and $7.5t_p$ in the spinful case at $U = 40t_p$ (Fig. 6). However, because of the artificial particle-hole symmetry, for $t_c/t_p < 0$ the locus of the transition is completely inconsistent with the spinful case, and the stability of the PL is widely overestimated.

We see from Fig. 6 that the effect of non-local inter-

actions V on the renormalization of the kinetic energy in the homogeneous metal is very similar in the spinful model at large U and in the spinless model, both being compatible with the quadratic V -dependence discussed above. We therefore conclude that the different behaviors observed in the two models at $t_c/t_p > 0$ are a direct consequence of the different kinetic energies at the *non-interacting* level, that results from the spurious particle-hole symmetry acquired by the spinless version.

The results presented here indicate that the charge rather than spin correlations dominate the renormalization effects on metallic properties approaching the charge order transition. However the spin multiplicity enters (indirectly) via the geometrical frustration, that is not treated correctly in the spinless model. A realistic spinful calculation therefore appears to be necessary to properly address the physics of θ -(ET) $_2$ X salts, where t_c/t_p is a key parameter in determining the experimental phase diagram^{20,36}.

IV. CORRELATED METAL AT FINITE TEMPERATURES

Here we analyze the properties of the homogeneous metallic phase at finite temperatures close to the QCP. A temperature scale emerges, that we denote T^* , above which the kinetic energy departs from Fermi liquid behavior and the specific heat coefficient goes through a maximum. We interpret T^* as a *renormalized Fermi temperature*, that generally drops to zero at the approach of the QCP. Such behavior is typically found for geometrical frustration $t_c \neq \pm t_p$. On the contrary, in cases in which there are competing Fermi surface instabilities, especially in the perfectly nested case $t_c = -t_p$, the T^* phenomenon is much weaker, and hardly affects the properties of the electron liquid. The data in that case are compatible with a Fermi temperature that remains finite right close to the QCP, possibly indicating that a first order transition may be occurring.

In the following paragraphs we focus specifically on the realistic value $U = 15t_p$, but the qualitative features presented here are unchanged for different large values of U .

A. Non-Fermi liquid behavior close to CO

1. Kinetic energy

The temperature dependence of the average kinetic energy K normalized to the non-interacting value K_0 ($U = V = 0$) is shown in Fig. 7 for $t_c/t_p = 1, 0.5, 0, -0.5, -1$. The different curves in each panel correspond to different values of the intersite Coulomb repulsion, V , across the charge ordering transitions. The ratios $t_c/t_p = 0.5, 0, -0.5$ (Fig. 7b, c and d) all show marked departures from the quadratic temperature dependence $K =$

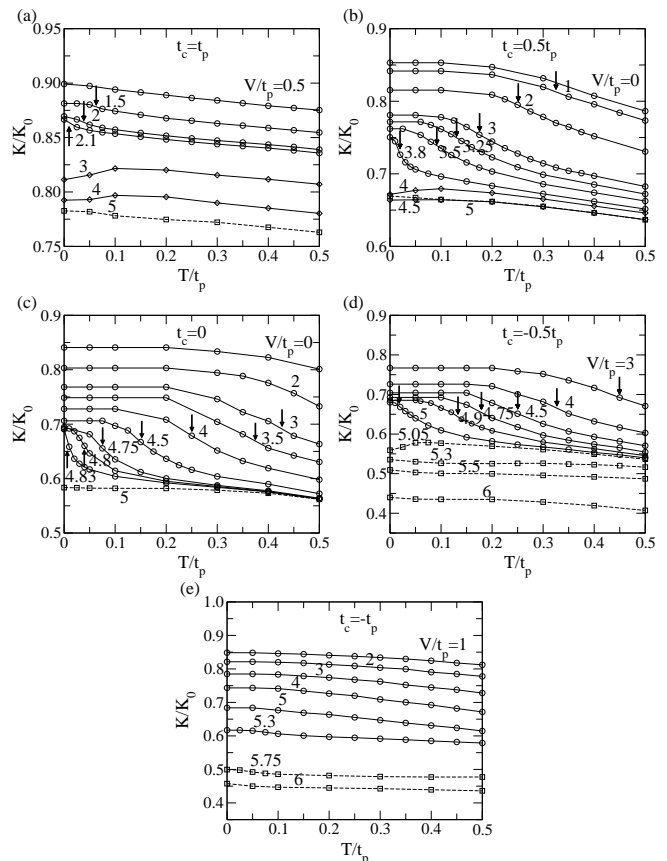


FIG. 7: Temperature dependence of the total kinetic energy at $U = 15t_p$ normalized to the non-interacting value K_0 , for $t_c/t_p = -1, -0.5, 0, 0.5$ and 1 . Arrows correspond to inflection points of the curves, indicating the temperature scale T^* corresponding to the breakdown of the quasiparticles. Open circles correspond to the HM phase, diamonds to the PL (full lines) and squares (dashed lines) to the 3CO phase.

$K_{T=0} - BT^2$ characteristic of conventional metals, occurring in the HM phase above a certain temperature (the approximate locus of the inflection points is indicated by arrows). We denote it as T^* and take it as an estimate of the renormalized Fermi temperature, governing a crossover to non-Fermi liquid behavior. Clearly, T^* is progressively reduced upon approaching the charge ordering transition and vanishes at the critical point. In this respect, our data in the experimentally relevant case $U = 15t_p$ do not show qualitative differences between the transition to the threefold charge order obtained for $t_c/t_p = -0.5; 0$ and that to the pinball phase for $t_c/t_p = 0.5$ (cf. Fig. 2): in both cases the temperature scale T^* appears to be entirely controlled by the approach to the zero-temperature ordering transition, indicating the possibility of quantum critical behavior at finite temperatures around the zero-temperature phase transition.

In the cases in which $t_c = \pm t_p$, the emergence of a temperature scale T^* is much less clear [Fig. 7 (a) and (e)] as the temperature dependence of the kinetic energy

is smooth within the whole homogeneous metallic phase except very close to the transition. Our RPA analysis presented in Appendix A shows that in these cases there is a competing CDW instability, that could indeed be masking the quantum critical behavior associated with the 3CO transition. For $t_c/t_p = -1$ the CDW is driven by the perfect nesting of the Fermi surface whereas for $t_c/t_p = 1$ a mixed CDW/CO phase induced by both nesting tendencies and strong Coulomb repulsion coexist.

The perfect nesting of the Fermi surface for $t_c/t_p = -1$ occurs at the wavevectors $\mathbf{Q}_F = (\pm\pi, \pm\pi/\sqrt{3})$ and $(0, \pm 2\pi/\sqrt{3})$. Such nesting instability is dominant at weak U , where it results in a striped charge modulation that dominates over the threefold charge order discussed above (this striped order is analogous to the checkerboard pattern obtained in the square lattice). Our data suggests that even in the presence of a sizable local Coulomb repulsion, $U = 15t_p$, that prevents the stabilization of such stripe order, an incipient nesting instability is strong enough to destroy the quantum criticality around the QCP. This conclusion is based on the observation that there is no clear signature of the vanishing low temperature scale, T^* , at the QCP and there is no clear evidence of the 'bad' metallic behavior found for other t_c/t_p ratios. However, there is a weak T -dependence of the kinetic energy that vanishes at a critical value $V_c = 6t_p$ as can be observed from the data of Fig. 7 (e). Such critical value, V_c , is found to be consistent with the critical value obtained from the 3CO charge correlations calculated below.

2. Charge correlations

The emerging QCP scenario can be further appreciated by studying the evolution of the charge ordering transition T_{CO} vs. temperature. This can be obtained by tracking the steepest variation of the charge correlation function, $C(\mathbf{Q})$ (arrows in Fig. 8a-d). In Fig. 9 we report T_{CO} together with the T^* extracted from figures 7, showing a common behavior in proximity to the CO instability. As stated in the preceding paragraph, the case $t_c/t_p = -1$ exhibits a different behavior, with no visible T^* approaching the QCP. The charge correlations (Fig. 8e) also exhibit a qualitatively different behavior in the perfectly nested case $t_c/t_p = -1$, with a mild non-monotonic temperature dependence showing a maximum at intermediate temperatures which suggests a 'reentrant' ordering transition. For this case, there is no clear indication of 'bad' metallic behavior in the kinetic energy and there is clear evidence of 'reentrant' behavior in the 3CO transition. This 'reentrant' behavior disappears at around the critical value $V_c = 6t_p$ as can be noted in Fig. 8d. It can be noted that a slightly reentrant behavior can be extracted from the data at $t_c/t_p = -0.5$. The presence of a reentrant behavior at negative values of t_c/t_p is confirmed by our RPA analysis, and is strongly reminiscent of what is commonly observed in the EHM

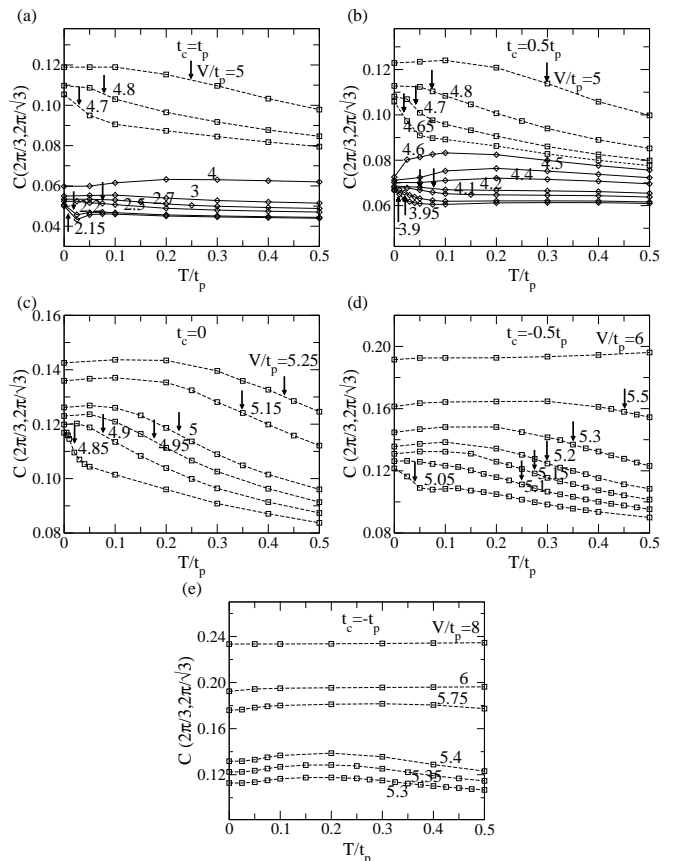


FIG. 8: Charge correlation function versus the temperature for different V/t in the CO phase at $U = 15t$ for $t_c/t_p = 1, 0.5, 0, -0.5, -1$. Arrows correspond to inflection points of the curves, indicating the ordering temperature T_{CO} .

on the square lattice (cf. Fig. 1 in Ref.¹⁴), which also in that case is ascribed to the competition of the CO phase with a Fermi surface nesting instability. We have added to the phase diagram for the case $t_c = -t_p$ the $2k_F$ -CDW instability and may also be present in other cases. However, the limited wavevector resolution of our small cluster calculation does not permit an accurate determination of the stability of the $2k_F$ -CDW phase. In fact, for $t_c = -0.5t_p$, we may also expect that CDW instabilities occur in the proximity of the 3CO instability.

3. Specific heat

Further insight on the anomalous properties of the homogeneous phase can be gained by exploring thermodynamic properties such as the temperature dependence of the specific heat coefficient C_V/T on approaching the QCP. In a Fermi liquid at low T , this quantity measures the effective mass enhancement of the quasiparticles. In Fig. 10 we compare C_V/T for $t_c/t_p = 0.5, -0.5, -1$. In this way we compare the behavior of the specific heat of a system across the 3CO ($t_c = -0.5t_p$) with a system

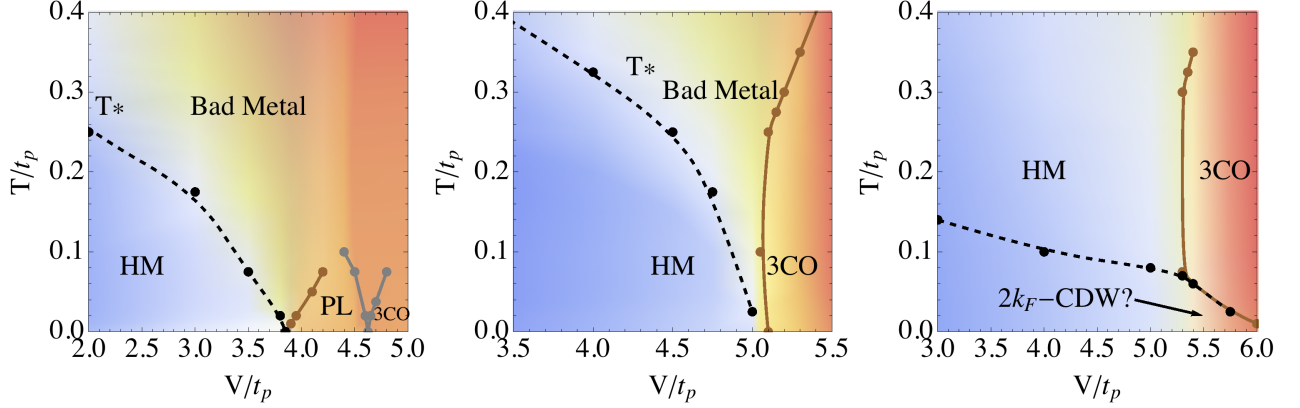


FIG. 9: (Color online) Color plots summarizing the QCP behavior at $U = 15t_p$ for the representative cases $t_c/t_p = 0.5, -0.5$ and -1 . The dashed curve is the renormalized Fermi temperature T^* extracted from Fig. 7. The full line is the charge ordering temperature T_{CO} extracted from Fig. 8. The color gradients (blue and red respectively) are derived from the kinetic energy and charge correlation data of Figs. 7 and 8.

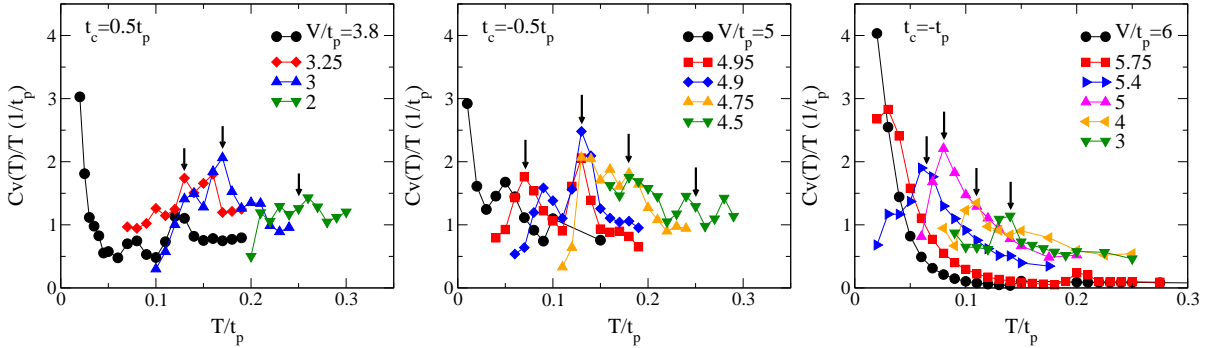


FIG. 10: (Color online) Temperature dependence of effective mass enhancement for different t_c/t_p ratios for $U = 15t_p$. A different behavior in the T -dependence is found for the case $t_c = -t_p$ for which T^* (indicated by the vertical arrows) which indicates a departure from the quantum critical behavior found in the other non-nested Fermi surface situations.

across the PL transition ($t_c/t_p = 0.5$). For completeness we also analyze the $t_c/t_p = -1$ case in which perfect nesting exists which can be compared to the other two cases. For both $t_c/t_p = \pm 0.5$ we find that a peak in C_V/T develops at T^* with $T^* \rightarrow 0$ on approaching the QCP as $V \rightarrow V_c$. This indicates that both the drop of T^* and the effective mass enhancement occurring in proximity to the QCP are consistent with the phase diagram of Fig. 9. Both effects are key signatures of the presence of a QCP together with the 'bad' metallic behavior arising around it.

The case $t_c = -t_p$ deserves special attention. For Coulomb repulsion energies up to about $V = 5.4t_p$, there is a moderate increase of the effective mass enhancements and a moderate shift of the peak to lower temperatures in contrast to previous cases. However, increasing V further leads to different behavior with a rapid increase of the effective mass enhancement and a shift of the peak to zero which indicates the proximity to a 3CO transition at $V_c = 6t_p$. The shift of the peak in the specific heat with V is plotted in the phase diagram of Fig. 9 together with the transition line to the 3CO. The two lines merge

and a clear 'reentrant' behavior of the 3CO transition is observed which is ascribed to the presence of the competing Fermi surface nesting instability. The origin of the specific heat peak is unclear since it does not separate the HM from the 'bad' metal and from Fig. 9 it is clear that the peak position has a different qualitative behavior for $t_c/t_p = -1$ than for other t_c/t_p ratios. In fact, there is no 'bad' metallic behavior in the HM phase as discussed previously. However, the fact that the effective mass is enhanced may indicate a transition to the $2k_F$ -CDW.

B. Connection with QCP physics

It is worth analyzing our numerical results from the perspective of the standard Moriya-Hertz-Millis (MHM)^{54,55} theory of quantum critical points (QCP). In principle, this theory could be appropriate to the transition from the HM to the 3CO phases considered here since both are metallic. However, one should keep in mind the limitations of the MHM theory. First, it is based on a weak coupling perturbative expansion around

the QCP. Second, the MHM theory is not applicable for ordering transitions which are driven by “ $2k_f$ ” Fermi surface instabilities. Hence, the MHM theory is applicable only to systems in which there is no nesting at all and for which the ordering wavevector \mathbf{Q} is not an extremal vector of the Fermi surface, *i. e.* loosely speaking $Q \neq 2k_f$. Our model satisfies the latter condition whenever $t_c/t_p \neq \pm 1$ for the 3CO wavevector: $\mathbf{Q} = (2\pi/3, 2\pi/\sqrt{3})$ (see Fermi surfaces and discussion in Appendix A). In these cases, the two-dimensional version of MHM, $d = 2$, with a dynamical scaling dimension, $z = 2$ (corresponding to nearly antiferromagnetic metals with effective dimension at the QCP: $D = d + z = 4$) is relevant. This situation corresponds to a marginal case which contains dangerously irrelevant operators in the renormalization group sense which can destroy the hyperscaling at the QCP. In this marginal case, $d = z = 2$, the Fermi liquid phase is bounded in the phase diagram by the condition: $T < r$, where $r = |V - V_c|$ quantifies the proximity to the QCP from the metallic side of the transition and V_c is the critical value at which CO occurs. The quantum critical region is bounded by the condition $T > r$ obtained from the scaling behavior of the renormalization group (RG) equations. A similar linear dependence with r is found in the boundary of the ordered phase which displays a critical non-Gaussian behavior around it due to the Coulomb interaction. As summarized in Fig. 9, for $t_c/t_p \neq \pm 1$ the suppression of T^* at the QCP and the ‘bad’ metallic behavior obtained at finite- T from our numerical calculations are qualitatively consistent with the MHM predictions for the marginal $d = z = 2$ case.

On the other hand, the extremal values: $t_c/t_p = \pm 1$ deserve special consideration. In the particular case: $t_c = -t_p$, the system has perfect nesting at the ordering wavevector: $\mathbf{Q}_F = (\pi, \pi/\sqrt{3})$, (see Fig. 11 in Appendix A) which describes diagonal stripe order in real space. A RPA analysis on the model shows that a CDW instability at \mathbf{Q}_F exists at small but finite U and V , which competes with the 3CO with $\mathbf{Q} = (2\pi/3, 2\pi/\sqrt{3})$. Such coexistence/competition between CDW and CO instabilities has also been found in RPA studies of the extended Hubbard model on the square lattice¹⁴. The situation in which two instabilities coexist—a nesting driven CDW with ordering vector \mathbf{Q}_F and a Coulomb driven instability with ordering vector \mathbf{Q} —has not been addressed in general at the level of the MHM approach. Our analysis shows that at moderate values of $U \gtrsim 7t_p$ nesting instabilities are washed away and the charge ordering transition is Coulomb driven. However, the competition washes out the T^* phenomenon and we find no clear evidence of ‘bad’ metallic behavior around the QCP in the case $t_c = -t_p$. This coincides with the breakdown of the MHM approach when nesting is present in the lattice.

We may speculate, based on our numerical analysis, that in the perfectly nested situations quantum criticality is destroyed and a first order transition occurs. Indeed, a somewhat related renormalization group (RG)

approach⁵⁶ to $2k_F$ -density wave quantum phase transitions in which curved Fermi surfaces with parallel tangents at two points of the Fermi surface connected by $2k_F$ are considered has found that critical fluctuations strongly influence the fermions on the Fermi surface and that the feedback effect of these fluctuations can destroy the second order quantum critical point turning it into a first order transition. Only in the special case in which $\mathbf{Q} = \mathbf{G}/2$, with \mathbf{G} being a reciprocal lattice vector, a second order quantum phase transition is recovered.

In actual quarter-filled organic materials, θ -ET₂X, for which hopping ratios $t_c/t_p \neq -1$ the MHM theory may be relevant. Many of the predictions for thermodynamic and transport properties in the quantum critical regime above the zero temperature QCP could be then experimentally checked. One important prediction of the MHM theory for $d = z = 2$ is the anomalous temperature dependence of the specific heat :

$$C \sim T \frac{\partial S}{\partial T} \Big|_V \sim T \ln 1/r, \quad T \ll r \quad (9)$$

$$T \ln 1/T, \quad T \gg r, \quad (10)$$

where r describes the proximity to the QCP. On the other hand, in clean nearly charge ordered two-dimensional metals the resistivity around the ‘hot’ spots in the quantum critical regime^{19,57} reads:

$$\rho \propto T^2, \quad T \ll r \quad (11)$$

$$T, \quad T \gg r. \quad (12)$$

However, the resistivity is shortcircuited by the contribution of electrons at the ‘cold’ spots since the scattering is small around these parts⁵⁸. Hence, the non-Fermi liquid behavior at the ‘hot’ spots is masked by the ‘cold’ sections eventually restoring Fermi liquid behavior: $\rho \sim T^2$. Therefore, within the MHM approach and in the the quantum critical region, the specific heat coefficient displays divergent behavior as $T \rightarrow 0$ following Eq. (10). The resistivity could show non-Fermi liquid behavior under small disorder which has been found to strongly influence antiferromagnetic QCP’s⁵⁹. Averaging the scattering rate over the Fermi surface reduces the effectiveness of the Hlubina-Rice mechanism and the scattering from the ‘hot’ regions becomes effective leading again to non-Fermi liquid behavior⁵⁹.

The behavior of the specific heat coefficient that we have found around the critical point (see Fig. 10) does show an enhancement on approaching the QCP in consistent agreement with Eq. (10). However, we cannot accurately determine the logarithmic dependence from our numerical data due to the small cluster sizes reached.

V. CONCLUSIONS AND OUTLOOK

We have analyzed in detail the effect of geometrical frustration on charge ordering transitions realized in

the extended Hubbard model on the anisotropic triangular lattice, which appropriately describes the family of quarter-filled layered organic crystals: θ -(ET) $_2$ X. The model contains both onsite, U , and inter-site Coulomb repulsion terms V_p and V_c , that are taken to be isotropic, $V_c = V_p = V$. The degree of geometrical frustration in the electron motion is tuned through the t_c/t_p ratio, which is an important parameter controlling the experimental phase diagram.

The zero temperature phase diagram of this model contains a homogeneous metal (HM), a pinball liquid (PL) and a three-fold charge ordered (3CO) phase. While the 3CO phase occurs at sufficiently strong inter-site interactions V for any fixed U , the PL only occurs above a certain threshold U value, as its existence is inherently tied up to the strong coupling regime. On the other hand, the PL is found to be stabilized by increasing the geometrical frustration of the lattice. Our results do show that in the range of values of U/t_p and V/t_p appropriate to the θ -(ET) $_2$ X materials, increasing the geometrical frustration of the lattice can effectively tune the system from a homogeneous metal (HM) with strong charge order correlations to a ‘‘pinball’’ liquid (PL) phase.

The phase transitions between charge ordered and disordered metallic phases can display quantum critical phenomena in close analogy with the heavy fermion systems^{16–19} with the critical charge rather than the spin fluctuations driving the CO transition. Such type of fluctuations may be at the origin of both the anomalous properties in the metallic state and Cooper-pair formation. Indeed, non-Fermi liquid behavior as well as non-BCS superconductivity have both been predicted and observed in quarter-filled organic materials of the α , β'' and θ -(ET) $_2$ X type^{60–64}. Such heavy fermion behavior arising from molecular π electrons instead of the d or f electrons, as occurs in the rare earths, may indeed find a natural explanation based on the properties of matter expected near a QCP.

In order to establish whether quantum critical behavior occurs or not in the quarter-filled layered materials close to CO several issues could be experimentally and theoretically addressed: (i) Is there evidence for the divergence of the specific heat coefficient and the quasiparticle effective mass, $m^*/m \rightarrow \infty$ and for the collapse of the Fermi temperature, $T^* \rightarrow 0$, near the QCP? Measurements of the quadratic coefficient of the resistivity approaching the QCP from the Fermi liquid side of the critical point can be useful to test the effective mass enhancement. Such type of experiments have been systematically performed in κ -(DHDA-TTP) $_2$ SbF $_6$ and (MeDH-TTP) $_2$ AsF $_6$, by tuning the system across the CO transition via applied pressure^{61,62}, yielding phase diagrams similar to those of Fig. 9. (ii) Is there non-Fermi liquid behavior of transport and thermodynamic properties in the quantum critical regime above the QCP? What is the temperature dependence of the resistivity in these systems? Are there clear deviations from Fermi liquid behavior of the form in Eqs. (10) and (12)? (iii) If quantum criticality and scal-

ing are observed in transport and thermodynamic quantities, how much of this behavior is consistent with the MHM predictions? Could there be a new universality class around the QCP in quasi-two-dimensional organic materials, related to the emergence of the pinball phase? (iv) Measurements of the Hall coefficient can be useful to disentangle whether the QCP is of the MHM type or different. In standard MHM theories, the Fermi surface would fold due to Bragg reflection off the density wave with no discontinuity in the Hall constant when the system is tuned across the QCP^{17,18}. However, as in heavy fermions a local type of QCP could arise in which the system jumps discontinuously from a large Fermi surface to a small Fermi surface through the QCP leading to a discontinuous jump of the Hall coefficient. Since the transition from the HM to the PL involves localization of the ‘pin’ electrons, a transition from the large Fermi surface of the HM involving all carriers to a small Fermi surface involving only ‘ball’ itinerant electrons could indeed occur. Understanding how this transition takes place and the type of QCP observed could be resolved by Hall constant measurements in analogy to the heavy fermion systems. (v) Here we have mainly discussed transitions between disordered and ordered *metallic* phases for which MHM theory is meant for. An important issue to address is how quantum criticality is modified in transitions from HM to CO *insulating* phases? This issue can be addressed within the EHM studied in the present work, by allowing for anisotropic Coulomb interactions $V_p \neq V_c$.

As observed in Ref.⁶⁵ the superconductivity in θ -(ET) $_2$ X compounds, as in other polytypes, frequently appears near to an insulator. In such cases, the cause of superconductivity (SC) may not be the simple weak coupling BCS mechanism by the electron-phonon interaction, but rather due to electronic correlations. Several theoretical works in the weak coupling limit have been performed in order to examine the possible mechanism for the onset of SC in proximity to the CO phase^{64,67,68}. Unconventional SC of the f -wave type has been encountered on the anisotropic triangular lattice with the model parameters: $t_c = 0$ and $V_c = V_p \approx t_p$ ³⁵ with $U = 10t_p$ and mediated by the charge fluctuations. This f -wave pairing symmetry is the analogous to the d_{xy} -wave pairing found in proximity to the checkerboard CO on the square lattice⁶⁴. It would be interesting to search for unconventional SC around the QCP found for other $t_c/t_p \neq 0$ ratios and U values both in the 3CO and PL type QCP. Based on the results of the present work, it can be conjectured that the anomalous properties and unconventional superconductivity observed in X=I $_3$ compounds maybe related to the proximity to the strong coupling PL phase since the onsite Coulomb repulsion energy is significant: $U = (15 - 20)t_p$. This could be tested by applying uniaxial pressure on the θ -(ET) $_2$ I $_3$ crystals.

Other materials such as the rare-earth nickelates, AgNiO $_2$, do show three-fold CO transitions similar to the one discussed here⁶⁹ although the origin of the CO transition may be non-Coulomb in origin since AgNiO $_2$ has

a complex multiorbital structure⁷⁰ and other effects such as Hund's coupling and crystal fields can play a relevant role. Thus, the organic materials of the θ -(ET)₂X type appear to be ideal candidates to single out the effects on electronic properties of metals close to a charge-driven quantum phase transition mediated solely by the onsite Coulomb repulsion between electrons at different sites.

Appendix A: RPA results at weak U

In the random phase approximation (RPA), the instability of the homogeneous metal is signalled by a divergence of the charge susceptibility¹⁴

$$\chi(\mathbf{q}) = \frac{\chi_0(\mathbf{q})}{1 + [U/2 + V(\mathbf{q})]\chi_0(\mathbf{q})} \quad (\text{A1})$$

at a given wavevector. Here $\chi_0(\mathbf{q})$ is the non-interacting susceptibility of the lattice, $V(\mathbf{q})$ is the interaction potential in Fourier space and U is the onsite repulsion. For isotropic n.n interactions on the triangular lattice we have

$$V(\mathbf{q}) = 2V \{ \cos(q_x) + \cos[(q_x + \sqrt{3}q_y)/2] + \cos[(q_x - \sqrt{3}q_y)/2] \}. \quad (\text{A2})$$

An instability occurs when the denominator in Eq. (A1) vanishes, which requires $-V(\mathbf{q}) = \chi_0^{-1}(\mathbf{q}) + U/2$. In principle the above equation can describe both *charge ordering*, driven by the Coulomb interaction $-V(\mathbf{q})$ that is maximum at the six equivalent threefold wavevectors $\mathbf{Q} = (\pm 2\pi/3, \pm 2\pi/\sqrt{3}), (\pm 4\pi/3, 0)$ (blue dot in Fig. 11a), and a charge density wave (CDW) induced by a large χ_0 . The evolution of the free-electron susceptibility with frustration is illustrated in Fig. 11b.

A CDW instability occurs for $t_c/t_p = -1$ due to a perfect nesting between parallel segments of the Fermi surface (red lines in Fig. 11a), at wavevector $\mathbf{Q}_F = (\pi, \pi/\sqrt{3})$ (red dot, corresponding to the \mathbf{M} -point), but is washed out at $U/t_p \gtrsim 7$, where the threefold order is always favored. An instability also appears to compete with the 3CO in the case $t_c/t_p = 1$ for $U \lesssim 2t_p$, at a wavevector $\mathbf{Q}_1 = (2.62, 2.72)$ (white dot). Such vector lies at the intersect between a circle of radius $|\mathbf{Q}_1| = 2k_F$ and the boundary of the Brillouin zone. It represents a compromise between a Fermi surface instability and a genuine charge ordering, as it benefits from both a large χ_0 and a large $-V(\mathbf{q})$. For values of the frustration ratio $|t_c/t_p| \lesssim 0.9$, the RPA predicts that the 3CO transition is dominant for all $U > 0$.

The critical coupling V_{3CO} at the threefold instability is shown as a function of the geometrical frustration in Fig. 11b. The RPA predicts an increase of V_{3CO} with t_c/t_p which originates from a decrease of the density of states at the Fermi level⁵³. We see that even at a relatively low value of $U = 5t_p$, the RPA result does not agree with the exact diagonalization data, showing an opposite trend for positive t_c/t_p ratios. In the ED, the t_c

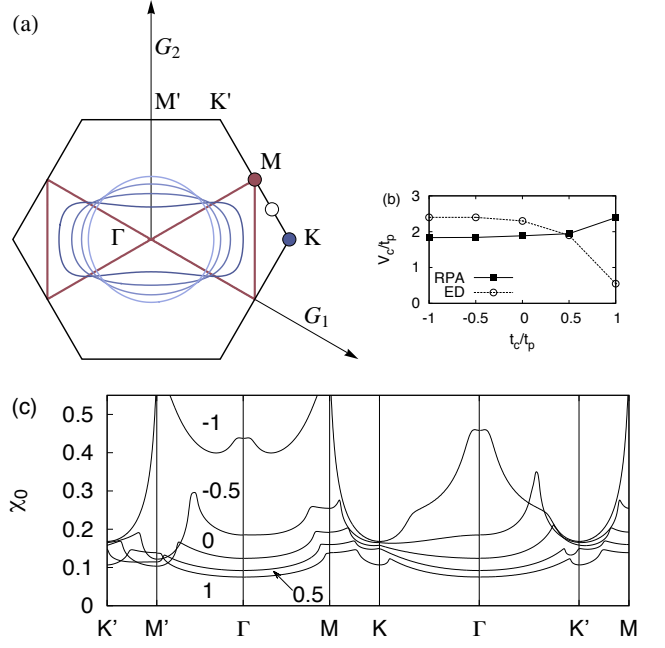


FIG. 11: (Color online) (a) Brillouin zone of the triangular lattice (black), reciprocal lattice vectors $G_1 = (2\pi, -2\pi/\sqrt{3})$ and $G_2 = (0, 4\pi/\sqrt{3})$ (arrows), and Fermi surface: from light blue to dark blue, $t_c/t_p = 1, 0.5, 0, -0.5$; red, $t_c/t_p = -1$ (same color code as in Fig. 2). The blue and red dots are respectively the threefold wavevector $\mathbf{Q} = \mathbf{K} = (4\pi/3, 0)$ and the nesting wavevector $\mathbf{Q}_F = \mathbf{M} = (\pi, \pi/\sqrt{3})$ connecting flat segments of the Fermi surface at $t_c/t_p = -1$ (red), while the white dot is the wavevector associated with the predominant instability for $t_c/t_p = 1$; (b) the critical value of the intersite Coulomb interaction V_{3CO} for $U = 5t_p$, comparing the RPA and ED results. (c) Free-electron susceptibility χ_0 along symmetry lines of the Brillouin zone, for different values of t_c/t_p .

dependence is governed by the stabilization of the pinball liquid phase, that is not captured by the weak coupling RPA argument.

Appendix B: Mean-field potential energy in the CO state

The Hartree expression for the potential energy per site in a charge ordered state with three-fold symmetry reads:

$$E_H = \frac{U}{3} (n_{A\uparrow}n_{A\downarrow} + n_{B\uparrow}n_{B\downarrow} + n_{C\uparrow}n_{C\downarrow}) + V(n_{AnB} + n_{AnC} + n_{BnC}). \quad (\text{B1})$$

We take $n_{A\uparrow} = n_{A\downarrow} = n_{B\uparrow} = n_{B\downarrow} = 1$, $n_{C\uparrow} = 1/2, n_{C\downarrow} = 0$ corresponding to the Hartree solution for the 3CO state and $n_{A\uparrow} = n_{B\uparrow} = 3/4, n_{A\downarrow} = n_{B\downarrow} = 1, n_{C\uparrow} = 1, n_{C\downarrow} = 0$ for the pinball liquid phase (see Fig.4). Inserting these

values in the preceding expression we find:

$$E_H^{(M)} = (9/16)U + (27/4)V, \quad \text{HM} \quad (\text{B2})$$

$$E_H^{(PL)} = (1/2)U + (13/2 + 1/16)V, \quad \text{PL} \quad (\text{B3})$$

$$E_H^{(3CO)} = (2/3)U + 6V, \quad \text{3CO} \quad (\text{B4})$$

The potential energy calculated by ED closely follows the V dependence predicted by the above mean-field equations (not shown). The transition from the pinball state to the three-fold CO state is well captured by the

mean-field analysis: the ED data closely follow the value $V_c = U/3$ obtained by equating $E_H^{(PL)} = E_H^{(3CO)}$.

Acknowledgements.

We acknowledge P. Horsch, A. Greco, A. Liebsch and M. Tamura for fruitful discussions. J.M. and L.C. acknowledge financial support from MICINN (CTQ-2008-06720-C02-02 and Consolider CSD2007-00010).

-
- ¹ V. J. Emery and S. A. Kivelson, Phys. Rev. Lett. **74**, 3253 (1995).
- ² J. Merino and R. H. McKenzie, Phys. Rev. B **61**, 7996 (2000).
- ³ P. B. Allen, Physica B **318**, 24 (2002).
- ⁴ N. E. Hussey, K. Takenaka, and H. Takagi, Philos. Mag. **84**, 2847 (2004).
- ⁵ M. Calandra and O. Gunnarsson, Phys. Rev. B **66**, 205105 (2002).
- ⁶ O. Gunnarsson, M. Calandra, and J. E. Han, Rev. Mod. Phys. **75**, 1085 (2003).
- ⁷ D. N. Basov, A. V. Chubukov, Nat. Phys. **7**, 272 (2011).
- ⁸ K. Miyagawa, A. Kawamoto, and K. Kanoda, Phys. Rev. B **61**, R7679 (2000).
- ⁹ K. Yamamoto, K. Yakushi, K. Miyagawa, K. Kanoda, and A. Kawamoto, Phys. Rev. B **65**, 085110 (2002).
- ¹⁰ M. Watanabe, Y. Nogami, K. Oshima, H. Mori, and S. Tanaka, J. Phys. Soc. Jpn. **68**, 2354 (1999).
- ¹¹ M. Watanabe, Y. Noda, Y. Nogami, and H. Mori, J. Phys. Soc. Jpn. **73**, 116 (2004).
- ¹² M. Watanabe, Y. Noda, Y. Nogami, and H. Mori, J. Phys. Soc. Jpn. **74**, 2011 (2005).
- ¹³ T. Mori, Bull. Chem. Soc. Jpn. **73**, 2243 (2000).
- ¹⁴ J. Merino, A. Greco, N. Drichko, and M. Dressel, Phys. Rev. Lett. **96**, 216402 (2006).
- ¹⁵ L. Cano-Cortés, J. Merino, S. Fratini, Phys. Rev. Lett. **105**, 036405 (2010).
- ¹⁶ K. Miyake, S. Schmitt-Rink, and C. M. Varma, Phys. Rev. B **34**, 6554 (1986).
- ¹⁷ P. Coleman, **1**: Fundamentals and Theory. John Wiley and Sons, 95-148 (2007);
- ¹⁸ P. Gegenwart, Q. Si, and F. Steglich, Nat. Phys. **4**, 186 (2008).
- ¹⁹ H. v. Löhneysen, A. Rosch, M. Vojta, and P. Wölfle, Rev. Mod. Phys. **79**, 1015 (2007).
- ²⁰ K. Kuroki Sci. Technol. Adv. Mater. **10**, 024312 (2009).
- ²¹ M. Udagawa and Y. Motome, Phys. Rev. Lett. **98**, 206405 (2007).
- ²² J. Jaklič, and P. Prelovšek, Phys. Rev. B. **49**, 5065 (1994).
- ²³ A. Liebsch, H. Ishida, and J. Merino, Phys. Rev. B **78**, 165123 (2008).
- ²⁴ A. Liebsch, H. Ishida, and J. Merino, Phys. Rev. B **79**, 195108 (2009).
- ²⁵ H. Seo, C. Hotta, and H. Fukuyama, Chem. Rev. **104**, 5005 (2004).
- ²⁶ H. Seo, J. Phys. Soc. Jpn. **69**, 805 (2000).
- ²⁷ M. Kaneko and M. Ogata, J. Phys. Soc. Jpn. **75**, 014710 (2006).
- ²⁸ K. Kuroki, J. Phys. Soc. Jpn. **75**, 114716 (2006).
- ²⁹ R. T. Clay, S. Mazumdar, and D. K. Campbell, J. Phys. Soc. Jpn. **71**, 1816 (2002).
- ³⁰ J. Merino, H. Seo, and M. Ogata, Phys. Rev. B **71**, 125111 (2005).
- ³¹ S. Nishimoto, M. Shingai, and Y. Ohta, Phys. Rev. B **78**, 035113 (2008).
- ³² T. Mori, J. Phys. Soc. Jpn. **72**, 1469 (2003).
- ³³ C. Hotta and N. Furukawa, Phys. Rev. B **74**, 193107 (2006).
- ³⁴ M. Miyazaki, C. Hotta, S. Miyahara, K. Matsuda, and N. Furukawa, J. Phys. Soc. Jpn. **78**, 014707 (2009).
- ³⁵ H. Watanabe and M. Ogata, J. Phys. Soc. Jpn. **75**, 063702 (2006).
- ³⁶ H. Mori, S. Tanaka, and T. Mori, Phys. Rev. B **57**, 12023 (1998).
- ³⁷ R. H. McKenzie, *et. al.* Phys. Rev. B **64** 085109 (2001).
- ³⁸ F. Nad, P. Monceau, H. M. Yamamoto, Phys. Rev. B **76**, 205101 (2007).
- ³⁹ M. Tamura, H. Kuroda, S. Uji, H. Aoki, M. Tokumoto, A. G. Swanson, J. S. Brooks, C. C. Agosta, and S. T. Hannahs, J. Phys. Soc. Jpn., **63**, 615 (1994).
- ⁴⁰ L. Cano-Cortés *et. al.*, Eur. Phys. J. B **56**, 173 (2007).
- ⁴¹ E. Scriven and B. J. Powell, J. Chem. Phys. **130**, 104 508 (2009).
- ⁴² H. Seo et al. J. Phys. Soc. Jpn., **75**, 051009 (2006). T. Mori, H. Mori, and S. Tanaka, Bull. Chem. Soc. Jpn. **72**, 179 (1999).
- ⁴³ A. J. Millis, *Optical Conductivity and Correlated Electron Physics, in Strong Interactions in Low Dimensions*, Edited by D. Baeriswyl and L. DeGiorgi, Springer Verlag, Berlin (2004).
- ⁴⁴ M. M. Qazilbash, J. J. Hamlin, R. E. Baumbach, L. Zhang, D. J. Singh, M. B. Maple, and D. N. Basov, Nat. Phys. **5**, 647 (2009).
- ⁴⁵ P. F. Maldague, Phys. Rev. B. **16**, 2437 (1977).
- ⁴⁶ G. Seibold, E. Sigmund, Z. Phys. B **101**, 405 (1996).
- ⁴⁷ C. Hotta, N. Furukawa, A. Nakagawa, and K. Kubo, J. Phys. Soc. Jpn. **75**, 123704 (2006).
- ⁴⁸ A. Ralko, *et. al.* Phys. Rev. B **74** 134301 (2006).
- ⁴⁹ A. Uhlmann, Rep. Math. Phys. **9**, 273 (1976).
- ⁵⁰ M. A. Nielsen and I. L. Chuang, *Quantum Computation and Quantum Information* (Cambridge University Press, Cambridge, 2000).
- ⁵¹ L. Campos Venuti and P. Zanardi, Phys. Rev. Lett. **99**, 095701 (2007).
- ⁵² P. Buonsante and A. Vezzani, Phys. Rev. Lett. **98**, 110601 (2007).

- ⁵³ S. Nishimoto and C. Hotta, Phys. Rev. B **79**, 195124 (2009).
- ⁵⁴ J. A. Hertz, Phys. Rev. B **14**, 1165 (1976).
- ⁵⁵ A. J. Millis, Phys. Rev. B **48** 7183 (1993).
- ⁵⁶ B. L. Altshuler, L. B. Ioffe, and A. J. Millis, Phys. Rev. B **52** 5563 (1995).
- ⁵⁷ A. Rosch, *et. al.* Phys. Rev. Lett. **79** 159 (1997).
- ⁵⁸ R. Hlubina and T. M. Rice, Phys. Rev. B **51** 9253 (1995).
- ⁵⁹ A. Rosch, Phys. Rev. Lett. **82** 4280 (1999).
- ⁶⁰ T. Ishiguro, K. Yamaji, and G. Saito, **1**: Organic Superconductors. Springer, New York, (2001), 2nd. ed.;
- ⁶¹ S. Yasuzuka, K. Kobayashi, H. Nishikawa, H. Yoshino, and K. Murata, J. Phys. Soc. Jpn., **75**, 083710 (2006).
- ⁶² Y. Weng, H. Yoshino, N. Hiratani, H. Akutsu, J. Yamada, K. Kikuchi, and K. Murata, Synth. Met. **159**, 2394 (2009).
- ⁶³ K. Takenaka, M. Tamura, N. Tajima, and H. Takagi, Phys. Rev. Lett. **95**, 227801 (2005).
- ⁶⁴ J. Merino and R. H. McKenzie, Phys. Rev. Lett. **87**, 237002 (2001).
- ⁶⁵ H. Mori, J. Phys. Soc. Jpn. **75**, 051003 (2006).
- ⁶⁶ M. Jourdan, M. Huth, and H. Adrian, Nature **398**, 47 (1999).
- ⁶⁷ D. J. Scalapino, E. Jr. Loh, and J. E. Hirsch, Phys. Rev. B **35**, 6694 (1987).
- ⁶⁸ Y. Tanaka, Y. Yanase, and M. Ogata, J. Phys. Soc. Jpn. **73**, 319 (2004).
- ⁶⁹ G. Pascut, *et. al.*, Phys. Rev. Lett. **106**, 157206 (2011).
- ⁷⁰ I. Mazin *et. al.*, Phys. Rev. Lett. **98**, 176406 (2007).
- ⁷¹ We work explicitly with electrons. To make contact with other theoretical works in the literature, the case $t_p < 0$ for $n = 3/2$ is equivalent to taking $t_p > 0$ for $n = 1/2$ (one-quarter filling) without changing the absolute sign of t_c .
- ⁷² In this work we consider the maximally frustrated case concerning interactions ($V_p = V_c = V$), while varying the degree of frustration in the electron motion via the parameter t_c/t_p . Previous studies of the EHM on the square lattice correspond, in the present language, to the case $V_p = V$ and $V_c = 0$.
- ⁷³ A word of caution is needed here since due to accidental degeneracies of the noninteracting kinetic energy, K_0 is independent of t_c/t_p in the small $N_c = 12$ cluster used which coincides with the $t_c = 0$ kinetic energy of the extended tight-binding model of the lattice. At $U > 5t$ degeneracies are split and dependence on t_c/t_p is recovered as expected.